Journal of Materials Chemistry A

PAPER

View Article Online
View Journal | View Issue

Cite this: J. Mater. Chem. A, 2016, 4, 13957

Nitrogen-rich microporous carbons for highly selective separation of light hydrocarbons†

Jun Wang,[ab] Rajamani Krishna,[c] Ting Yang[b] and Shuguang Deng*[ab]

Received 13th June 2016
Accepted 8th August 2016

DOI: 10.1039/c6ta04939g

www.rsc.org/MaterialsA

A controllable and facile one-pot method for synthesizing N-doped activated carbons (NACs) with a considerable amount of N by using a nitrogen-rich polymer precursor as both the nitrogen source and self-template is reported. The obtained NACs are promising solid adsorbents for light hydrocarbon separations with tunable microstructures. Particularly, NACs with a narrow pore size distribution (*ca.* 2.6–3.8 nm), high specific surface area (*ca.* 1628.9–2146.1 m^2 g^{-1}), and high heteroatom content (*ca.* 3.6 wt%) exhibited excellent hydrocarbon uptake capacities (*ca.* C2 7.59 mmol g^{-1} and C3 11.77 mmol g^{-1}). Remarkably, NACs also showed unprecedented C3/C2/C1 separation selectivity (*ca.* C2/C1 65.7 and C3/C1 501.9) at 298 K and 1.0 bar, which is one of the highest so far reported for benchmark adsorbents, according to the ideal adsorbed solution theory (IAST). Combined with its simple preparation, high adsorption capacity, and excellent light hydrocarbon selectivity, the sample NAC 700 is a potent and promising solid-state adsorbent for light hydrocarbon separation.

1 Introduction

Light hydrocarbons are very important alternative energy sources and raw chemicals. Therefore, it is urgent to develop materials and methods for efficient separation and purification of light hydrocarbon mixtures. Among the feasible fossil energies, natural gas, which comprises primarily methane and varying amounts of impurities, such as CO_2, H_2O, C_2H_2, C_3H_6, *etc.*, is regarded as a promising alternative fuel because it is naturally abundant and environmentally friendly compared to controversial petrol and diesel.[1] Moreover, hydrocarbons are important raw chemical materials for manufacturing major industrial polymers, such as polyethylene, polypropylene, polyester, and polystyrene. However, C1 to C3 light hydrocarbons, CH_4, C_2H_2, C_2H_4, C_2H_6, C_3H_6, and C_3H_8, are found mixed in natural gases or petroleum products. Therefore, it is essential to separate such light hydrocarbons to fully utilize them. The traditional separation and purification of these feedstocks are carried out by the cryogenic distillation method, which is not only very energy intensive but also requires harsh operating conditions, such as high pressure and low temperature. Hence, exploiting more energy-efficient technologies is highly desirable. Among many new developed technologies, pressure swing adsorption (PSA) is a low-cost and energy-saving method.

The first-generation adsorbents considered for light hydrocarbon separation are zeolites;[2] however, these zeolites possess an average kinetic diameter of 8–10 Å, which is larger than the molecular size of hydrocarbons, resulting in inferior separation performance.[3] Therefore, other porous materials have been investigated for hydrocarbon separations including molecular sieves[4] and porous coordination polymers (PCPs),[5] and achieved better performance. Very recently, a new adsorbent synthesis approach has been developed to enhance gas adsorption capacity and separation selectivity by tailoring surface chemistry, tuning the pore size and shape, and utilizing structural flexibility.[6] Amongst porous materials, metal–organic frameworks (MOFs) have been employed as a novel class of designable adsorbents and have attracted extensive research interest in hydrocarbon separation.[7] The potential of MOFs has been well established for a variety of light hydrocarbon separations, such as C_2H_2/C_2H_4,[8] C_2H_4/C_2H_6,[9] $CH_4/C_2H_2/C_2H_4/C_2H_6$,[7a,10] and $CH_4/C_2H_2/C_2H_4/C_2H_6/C_3H_8$ mixtures.[7a,11] However, MOFs are relatively expensive to manufacture and unstable under certain operating conditions. In contrast, microporous activated carbons (MACs) have been considered as very promising materials, due to their low fabrication cost, inertness to moisture, and high adsorption capacity. MACs are usually exploited for selective adsorption of CO_2 over CH_4,[12] N_2,[13] and H_2.[14] However there are very limited published studies on MACs compared to MOFs for light hydrocarbon separation. Until most recently, algae-derived carbons have been explored to separate C_2H_6/CH_4 with a moderate C2 capacity and selectivity.[15] In line with this, we have designed and prepared a novel class of

[a]School of Environmental and Chemical Engineering, Nanchang University, Nanchang 330031, Jiangxi, PR China

[b]School for Engineering of Matter, Transport and Energy, Arizona State University, 531 E. Tyler Mall, Tempe, AZ, 85287, USA. E-mail: shuguang.deng@asu.edu; Tel: +1-480-727-7238

[c]van't Hoff Institute for Molecular Sciences, University of Amsterdam, Science Park 904, 1098 XH Amsterdam, The Netherlands

† Electronic supplementary information (ESI) available. See DOI: 10.1039/c6ta04939g

nitrogen-doped MACs for the selective separation of light hydrocarbons (C1–C3).

Separating CH_4 from other hydrocarbons is comparatively easier, due to its smaller molecular size and non-polarity. The weaker interaction force between CH_4 and adsorbents makes selective adsorption separation possible, whereas separations of C_2H_2/C_2H_4, C_2H_4/C_2H_6, and C_3H_6/C_3H_8 are much more difficult, because these molecules have very similar molecular sizes and other properties.[16] It is even more challenging to separate C1/C2 and C1/C2/C3 mixtures.[17]

In this study, a series of nitrogen-doped hierarchical microporous carbons (NACs) were prepared from a nitrogen-rich polymer precursor followed by KOH activation. The light hydrocarbon separation and storage ability of NACs were investigated based on inspection of their pure-component adsorption isotherms. Pre-doped nitrogen functionalization is preserved to enhance the molecular adsorption capacity and selectivity. Additionally, we demonstrated that the NACs could be utilized as potent adsorbents for light hydrocarbon selective adsorption. Furthermore, breakthrough simulation, pulse chromatographic simulation, isosteric adsorption heat, and IAST selectivity were conducted, calculated and presented properly on equimolar 4- and 6-component mixtures, which strongly support our conclusion as well.

2 Experimental section

Adsorbent sample preparation

In a typical synthesis run, terephthalaldehyde (TTD) (3 g) was dispersed in 50 mL dichloroethane (DCE) at room temperature using sonication. Ethylenediamine (EDA) (8 g) dissolved in 50 mL DCE was added to this solution. 5 g of formic acid was added as a catalyst. The resulting solution was stirred and allowed to polymerize for 24 hours at 100 °C and 48 hours at 170 °C. After cooling to room temperature, insoluble solids were removed by filtration, and washed several times with methanol and deionized (DI) water. The precipitate was then re-suspended in 100 mL 1 M HCl at room temperature for 3 h. The solution was filtered and the precipitate was washed with DI water until neutral pH was obtained. Finally, the yellow solid products were dried at 80 °C under vacuum for 24 h.

The chemical activation of NACs was carried out using a 1 : 2 ratio of the precursor to potassium hydroxide (KOH). Typically, 1.5 g polymer material and 3 g of KOH were mixed and ground to produce a uniform powder. The mixture in an alumina boat was placed in a horizontal furnace under a nitrogen flow (100 mL min^{-1}) and heated (3 °C min^{-1}) to temperatures ranging from 600 to 800 °C and held for 1 hour. After cooling in nitrogen flow, the obtained carbon material was washed with 8% HCl and DI water until neutral pH was observed, and dried under vacuum at 80 °C for 24 h. The resulting N-doped carbons were designated as NAC x, where x is the carbonization temperature (°C). The schematic illustration of the synthesis process is presented in Fig. S1.†

Characterization

NACs were characterized using small-angle X-ray diffraction (SXRD) (Bruker AXS D8 diffractometer with Cu Kα radiation at 40 kV high tension), scanning electron microscopy (SEM) (NOVA 200 Nanolab SEM at 10 kV equipped with energy-dispersive X-ray analysis), high resolution transmission electron microscopy (HR-TEM) (JOEL 2010F at 200 kV), X-ray photoelectron spectroscopy (XPS) (VG ESCALAB 220i-XL with an Al Kα anode), Brunauer–Emmett–Teller (BET) surface area analysis (Micromeritics ASAP 2020 adsorption apparatus), Raman spectroscopy (Renishaw Raman microscope with 532 nm, 50 mW laser excitation), thermal gravimetric analysis (TGA) (PerkinElmer Thermogravimetric Analyzer), and ultimate analysis (PE 2400 Series II CHNS/O Analyzer).

Adsorption isotherm measurements

The pure component adsorption isotherms of CH_4, C_2H_2, C_2H_4, C_2H_6, C_3H_6, and C_3H_8 at three temperatures (273, 298,

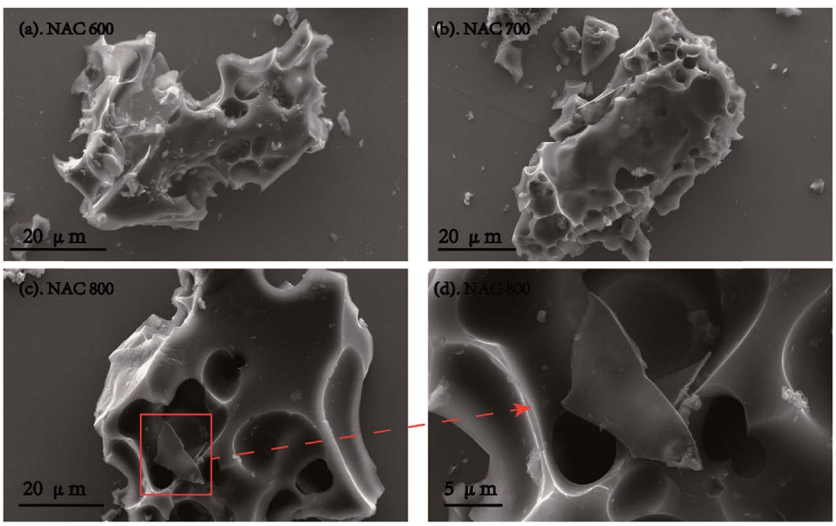

Fig. 1 SEM images of (a) NAC 600, (b) NAC 700, (c) NAC 800 at the 20 μm scale, and (d) NAC 800 at the 5 μm scale.

and 323 K) and gas pressure up to 800 mmHg were measured volumetrically in the Micromeritics ASAP 2020 adsorption apparatus. All temperatures were achieved by using a Dewar with a circulating jacket connected to a thermostatic bath with a precision of ±0.01 °C. The degassing procedure was repeated in all samples before measurements at 250 °C for 24 h. Ultrahigh purity grade CH_4, C_2H_2, C_2H_4, C_2H_6, C_3H_6, and C_3H_8, and He from Matheson Co. were used as received. The Brunauer–Emmett–Teller (BET) surface area was calculated between 0.05 and 0.3 relative pressure and pore size distributions were calculated using Non-Local Density Functional Theory (NLDFT) from N_2 adsorption–desorption isotherms measured at 77 K.

3 Results and discussion

Structure and surface texture properties

The SEM images of NACs, shown in Fig. 1, clearly demonstrated a typical hierarchical surface and numerous holes (with diameters about 5 μm) in a honeycomb shape. These irregular cottony holes were surrounded by contracted and twisted walls. The aggregation of carbon particles in the form of blocks 30 to 50 μm in size was observed. It must be pointed out that carbon sheet existed at higher annealing temperatures (Fig. 1c and d). This phenomenon is further confirmed by the HR-TEM images (Fig. 2), revealing that the particles are composed of stacked carbon sheets. It is observed in experiments that the higher the

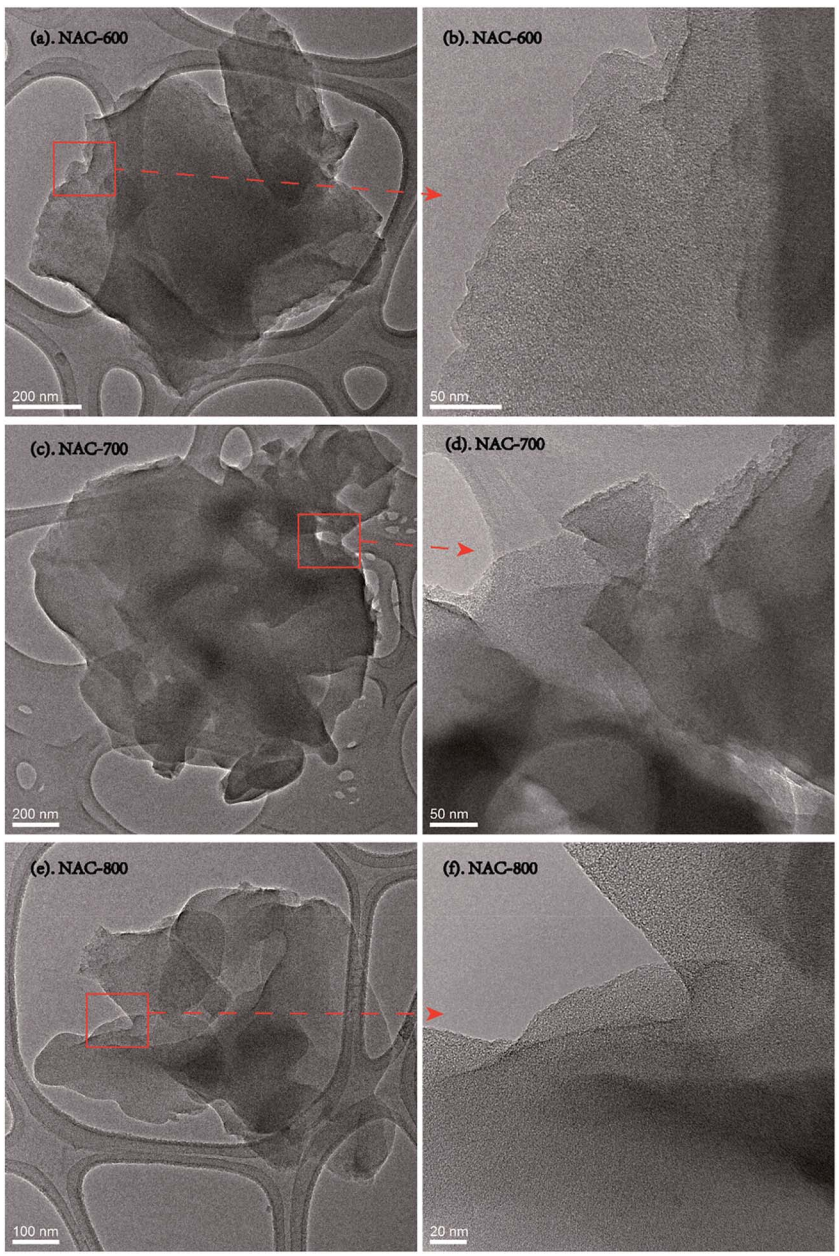

Fig. 2 HR-TEM images of (a) NAC 600 at the 200 nm scale, (b) NAC 600 at the 50 nm scale, (c) NAC 700 at the 200 nm scale, (d) NAC 700 at the 50 nm scale, (e) NAC 800 at the 100 nm scale, and (f) NAC 800 at the 20 nm scale.

pyrolysis temperature is, the more the characteristic layered structures of carbon particles will be. Furthermore, the HR-TEM images also indicated the presence of an amorphous and uniformly distributed pore structure of NACs.

The SXRD pattern (Fig. 3) of NACs revealed three well-resolved broad scattering peaks centered at $2\theta = 0.4$, 0.7, and 1.3°, equivalent to a lattice spacing of 22.1, 12.6, and 6.8 nm, respectively. This implied that the obtained hybrid carbons possess molecular homogeneity locally and a long-range order, although the degree of the order is not very high.[18] The wide XRD patterns are presented in Fig. S2,† with two broad peaks centered at $2\theta = 22$ and 43°, which could be indexed to (002) and (100) reflections, respectively.[19] The d_{002}-spacing distance was calculated to be 2.98 Å, exhibiting a smaller d_{002}-spacing than that for natural graphite of 3.35 Å.[20] The relatively broad peaks revealed that NACs possessed low crystallinity, which is well in accordance with Raman spectral patterns as shown in Fig. 3b, where all samples exhibited two distinctive bands, corresponding to the D band at 1355 cm^{-1} and the G band at 1583 cm^{-1}. The D band is often referred to as the disorder band, associated with defect-induced mode, while the G band is referred to as the ordered band, corresponding to the E_{2g} mode of graphite.[21] By determining the area under the peak for the D- and G-bands, I_D/I_G values, which represent the ratio of amorphous to graphitic carbon, were estimated to be 0.56, 0.87, and 0.95, respectively. The value of the lattice distance (L_a) can be calculated from the following equation:[22]

$$L_a\ (\text{nm}) = (2.4 \times 10^{-10})\lambda^4 (I_D/I_G)^{-1} \quad (1)$$

where λ is the wavelength of the laser line in nm, which is 532 nm in this case. The L_a values were calculated to be 34.3, 22.1, and 20.2 nm, respectively. The presence of the characteristic 2D band (2680 cm^{-1}) further indicated a few-layer graphene-like structure.[23] This is consistent with the HR-TEM observation. The thermal behavior and stability of NACs were further investigated by TGA (Fig. S3†), the thermograms demonstrated that the mass loss occurred around 100 °C attributed to desorption of a small amount of moisture and air and NACs are thermally stable up to a temperature of 850 °C, which is sufficient to treat outgas from industry directly.

Table 1 summarizes the chemical compositions of NAC materials characterized by the ultimate elemental analysis and XPS, and the main composition was found to be C, N, and O. The content of heteroatoms (N and O) gradually decreases with respect to increasing carbonization temperature. The N 1s XPS spectra of NACs, shown in Fig. 4, exhibited a broad peak at 400.1 eV, and this peak could be deconvoluted into two distinct peaks at 398.6 and 400.8 eV, with the area ratio = 1 : 5.3, 1 : 2.4, and 1 : 11.2 for NAC 600, NAC 700, and NAC 800, respectively. These two peaks belong to pyridinic and quaternary nitrogen species.[24] The C 1s XPS results further support the successful formation of carbonaceous materials (Fig. S4†). A strong signal centered at 284.9 eV was detected, which could be deconvoluted into three distinct peaks. The spectrum of NAC 600 and NAC 700, shown in Fig. S4a and b,† revealed the presence of signals for CHO (284.9 eV), CNH_2 (286.0 eV), and O=C–O (288.6 eV), whereas the spectrum of NAC 800 (Fig. S4c†) could be deconvoluted into CHO (284.9 eV), –C=O (287.2 eV), and CO_3^- (290 eV) peaks, which implies diminution of N species at high activation temperature.

The nitrogen adsorption experiment at 77 K was conducted to probe the porosity of activated carbon materials. As shown in Fig. 5a, all NACs exhibited a steep nitrogen adsorption at low pressure ($P/P_0 < 0.05$), which is indicative of the abundantly developed micropores and a typical type I isotherm, according to the IUPAC classification.[25] It is worth noting that the "knee" of nitrogen adsorption isotherms gradually widened as the activation temperature increased. This implies a broadening of the corresponding average pore size. The corresponding NLDFT

Table 1 Chemical composition of NACs determined by ultimate elemental analysis and XPS

	Ultimate element analysis (wt%)			XPS (atom%)		
Samples	C	O	N	C	O	N
NAC 600	76.6	17.6	3.6	76.8	19.2	4.0
NAC 700	78.4	18.2	3.5	82.0	14.2	3.3
NAC 800	74.6	21.9	2.4	87.2	10.4	2.4

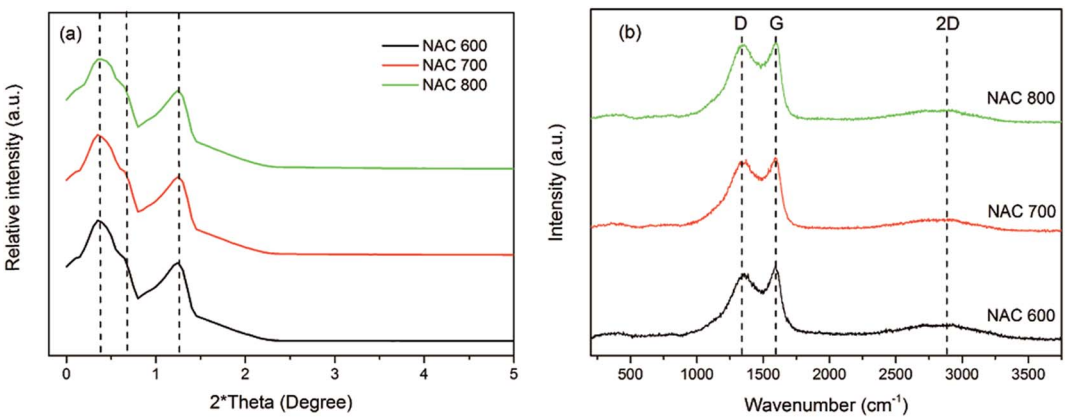

Fig. 3 (a) SXRD patterns and (b) Raman spectra of NACs.

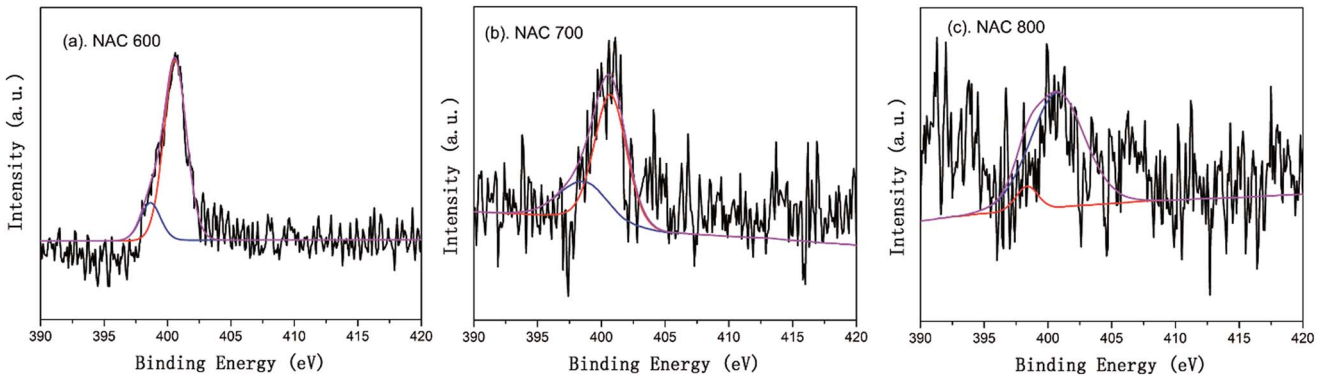

Fig. 4 N 1s spectra of (a) NAC 600, (b) NAC 700, and (c) NAC 800.

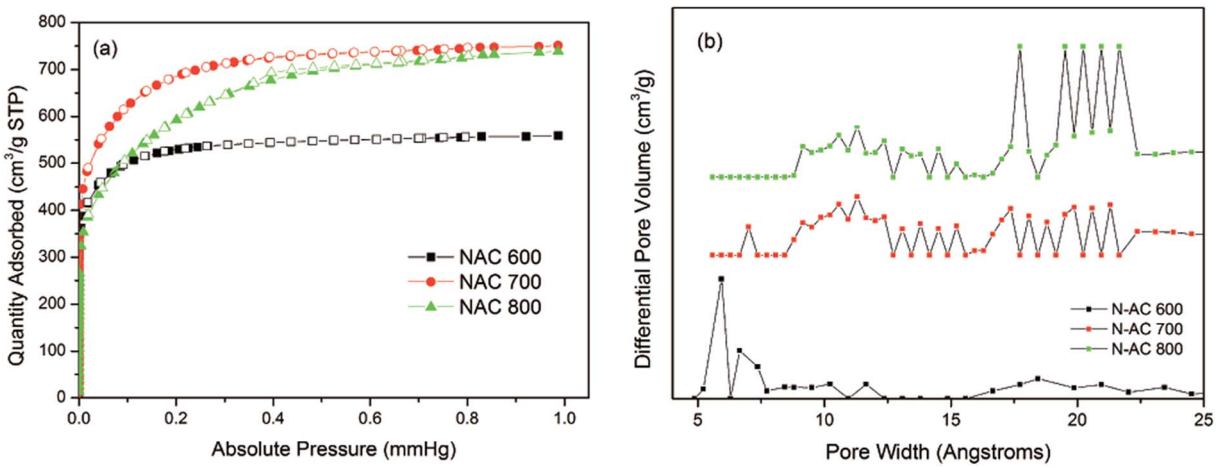

Fig. 5 (a) N_2 sorption isotherms at 77 K and (b) NLDFT pore size distribution of NACs.

differential pore volumes as a function of pore width are given in Fig. 5b. These curves definitely confirm that NACs were microporous frameworks. Consequently, NACs possessed a BET surface area of 1628.9, 2146.1, and 1942.8 $m^2\ g^{-1}$, for NAC 600, NAC 700 and NAC 800, respectively, which is summarized in Table 2. It is noted that NAC 700 displayed the largest total pore volume of 1.96 $cm^3\ g^{-1}$, whereas the micropores only accounted for 46.4%.

Light hydrocarbon adsorption and isosteric heat of adsorption

To examine the light hydrocarbon adsorption and separation performance of NACs, single component gas adsorption isotherms for various light hydrocarbons (CH_4, C_2H_2, C_2H_4, C_2H_6, C_3H_6, and C_3H_8) were measured at 273, 298 (Fig. 6), and 323 K (Fig. S5†), and the dual-site Langmuir–Freundlich model fitting parameters are listed in Tables S1–S3.† One interesting feature is that NACs displayed three distinguishable adsorption zones in the following trend: C3 > C2 > C1, due to the hierarchy of adsorption strengths, making separation of heavier hydrocarbons from methane and selective fractionation of these small hydrocarbons according to the carbon atom number feasible. In practical applications, separations of these light hydrocarbons are conducted in a pressure swing adsorption (PSA) process. It is widely acknowledged that the separation characteristics are determined by not only adsorption separation factors but also the adsorption uptake capacities.[7a] A

Table 2 Textural properties of porous carbon materials[a]

Samples	S_{BET} ($m^2\ g^{-1}$)	S_{micro} ($m^2\ g^{-1}$)	S_{lang} ($m^2\ g^{-1}$)	V_p ($cm^3\ g^{-1}$)	V_{micro} ($cm^3\ g^{-1}$)	D_{aver} (nm)
NAC 600	1628.9	1859.8	2455.4	0.86	0.77	2.6
NAC 700	2146.1	2132.7	3333.1	1.96	0.91	3.2
NAC 800	1942.8	1695.1	3373.9	1.14	0.73	3.5

[a] Apparent specific BET surface area calculated in the P/P_0 range of 0.005 to 0.3. Total pore volume at $P/P_0 = 0.99$; micropore volume determined from the nitrogen adsorption isotherm at 77 K using the D–R equation. Average pore diameter calculated by the BJH method.

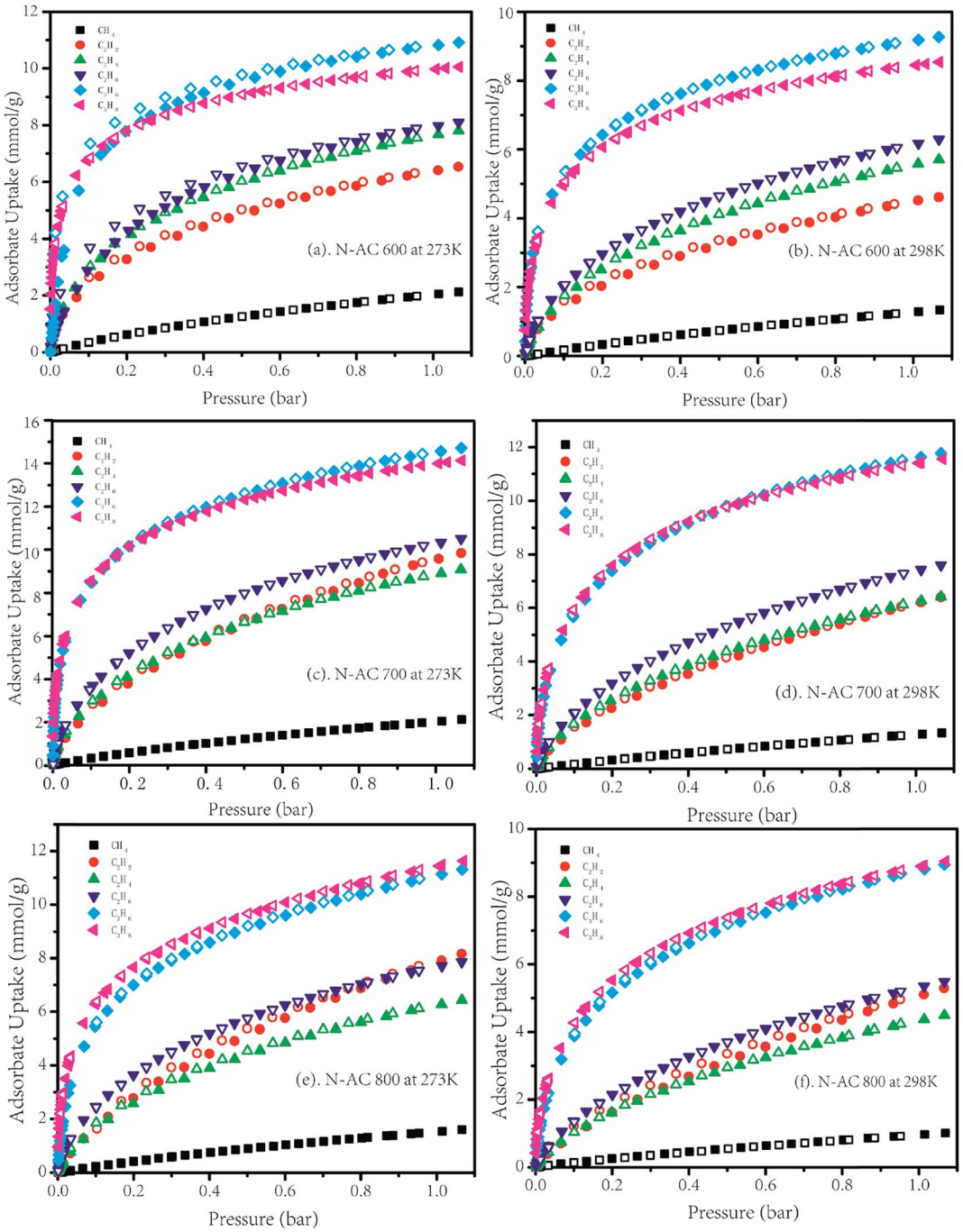

Fig. 6 Light hydrocarbon adsorption isotherms on NAC 600 at (a) 273 K and (b) 298 K, NAC 700 at (c) 273 K and (d) 298 K, and NAC 800 at (e) 273 K and (f) 298 K.

common thought is that higher capacities provide a longer operation time before the regeneration arises in the adsorber bed. As expected, NCA 700 exhibited a very high uptake of C_2H_2 (6.39 mmol g^{-1}), C_2H_4 (6.41 mmol g^{-1}), C_2H_6 (7.59 mmol g^{-1}), C_3H_6 (11.77 mmol g^{-1}), and C_3H_8 (11.56 mmol g^{-1}) at 298 K and 1 bar but a much smaller amount of CH_4 (1.33 mmol g^{-1}), indicating that NACs are extremely promising materials for highly selective adsorption separation of C3 and C2 hydrocarbons over CH_4. The adsorption capacities are summarized in Table 3. This unprecedented uptake capacity outperformed that of other outstanding porous materials such as ZJU-48a,[7b] FJI-C4,[7c] [Cu(dhbc)$_2$(4,4′-bipy)],[7d] and UTSA-35a.[26] It should be noted that the adsorption capacity of C2 is at least two times higher and that of C3 is at least three times higher than the corresponding values in published studies.[7,26] The regeneration ability of the N-doped carbons has been examined as well and the adsorption capacities are almost identical in three cycle tests (Fig. S6†). The superior adsorption capacity could be accredited to the large surface area, suitable pore size distribution and *N* functional groups.

Table 3 Hydrocarbon adsorption capacities on NACs at 298 K and 273 K in parentheses

Sample	NAC-600 (mmol g^{-1})	NAC-700 (mmol g^{-1})	NAC-800 (mmol g^{-1})
CH_4	1.33(2.12)	1.33(2.11)	1.00(1.59)
C_2H_2	4.60(6.53)	6.39(9.86)	5.28(8.16)
C_2H_4	5.70(7.81)	6.41(9.09)	4.49(6.43)
C_2H_6	6.29(8.10)	7.59(10.52)	5.84(7.87)
C_3H_6	9.25(10.92)	11.77(14.74)	8.94(11.31)
C_3H_8	8.53(10.05)	11.56(14.16)	9.04(11.64)

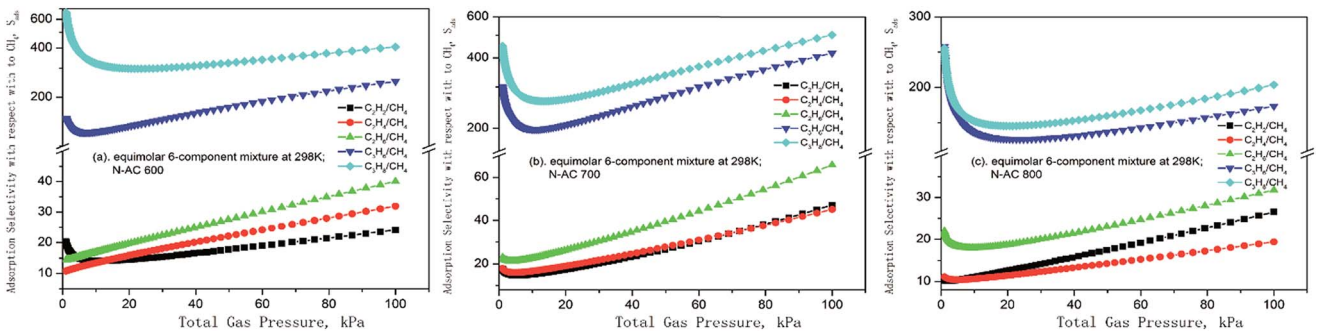

Fig. 7 IAST calculations of C3/C1 and C2/C1 in an equimolar 6-component $CH_4/C_2H_2/C_2H_4/C_2H_6/C_3H_6/C_3H_8$ mixture on (a) NAC 600, (b) NAC 700, and (c) NAC 800 at 298 K and 1 bar.

To evaluate the affinity of the pore surface towards the adsorbates on NACs, the isosteric heat of adsorption was calculated by the Clausius–Clapeyron equation, defined as

$$Q_{st} = RT^2\left(\frac{\partial \ln p}{\partial T}\right)_q \quad (2)$$

Table 4 IAST selectivity of C2/C1 and C3/C1 on NACs at 298 K and 1 bar

Sample	NAC-600	NAC-700	NAC-800
C_2H_2/CH_4	24.2	47.1	26.5
C_2H_4/CH_4	31.9	45.1	19.4
C_2H_6/CH_4	40.0	65.7	31.8
C_3H_6/CH_4	248.7	419.8	173.6
C_3H_8/CH_4	406.0	501.9	203.6

The values were determined using the pure-component isotherm fitted at 273, 298 and 323 K. The adsorption heat for CH_4, C_2H_2, C_2H_4, C_2H_6, C_3H_6, and C_3H_8 was in the range of 17.4–18.2 kJ mol^{-1}, 19.8–27.0 kJ mol^{-1}, 22.1–24.7 kJ mol^{-1}, 23.9–24.4 kJ mol^{-1}, 20.7–31.9 kJ mol^{-1} and 30.5–33.8 kJ mol^{-1} (Fig. S7†), respectively. The higher adsorption heats of heavier hydrocarbons can be ascribed to the larger van der Waals interactions between the carbon network and hydrocarbon molecules. Moreover, the nitrogen functionalization generates even stronger interactions with those easily polarized hydrocarbons.

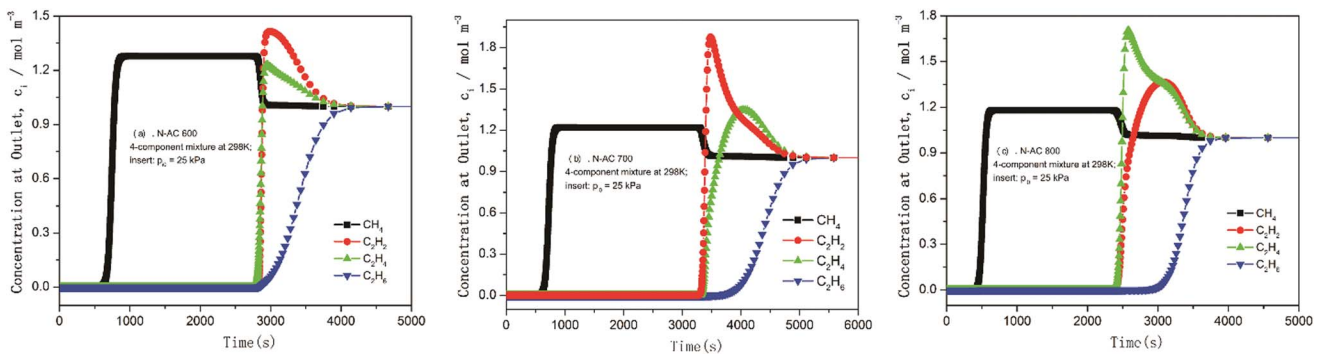

Fig. 8 Breakthrough simulation curves of (a) NAC 600, (b) NAC 700, and (c) NAC 800, for separation of an equimolar 4-component $CH_4/C_2H_2/C_2H_4/C_2H_6$ mixture in a fixed adsorber at 298 K and 1 bar.

Gas separation properties

The higher adsorption heat on C2–C3 hydrocarbons implied a stronger affinity with the carbon skeleton, which causes these gases to be preferentially adsorbed. Thus, a high selectivity of C2–C3 hydrocarbons with respect to CH_4 could be anticipated. The IAST method was applied to appraise the potential for light hydrocarbon separations from an equimolar 6-component mixture (Fig. 7). At 298 K and 1 bar, the highest selectivities were obtained for NAC 700, where the selectivities of C_2H_2, C_2H_4, C_2H_6, C_3H_6, and C_3H_8 with respect to CH_4 are 47.1, 45.1, 65.7, 419.8 and 501.9, respectively. The values are summarized in Table 4. The calculated selectivities are much higher than the corresponding values of FJI-C4,[7c] UTSA-35a[26] and many other benchmark adsorbents (Table S4†).[27] Noticeably, the selectivity of C_3H_8/CH_4 (501.9) is even better than the current highest values of FJI-C1 (471).[28] This result strongly supported the fact that NAC 700 is a potent adsorbent for effective selective adsorptive separation of CH_4 from C2–C3 light hydrocarbons under ambient conditions.

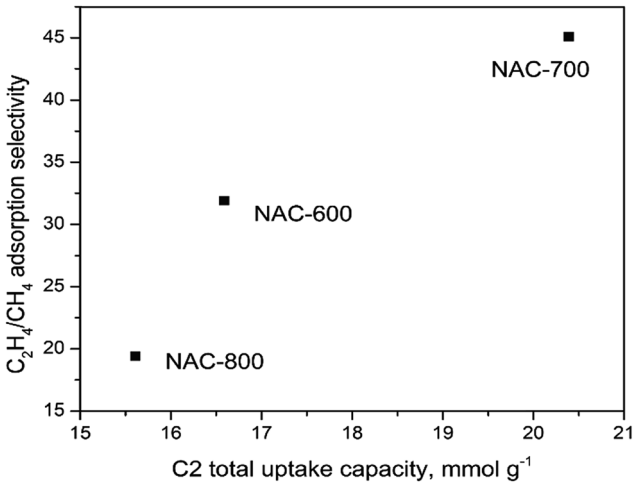

Fig. 9 IAST calculations of the C_2H_4/CH_4 adsorption selectivity *versus* the total C2 uptake capacity for adsorption from an equimolar 4-component mixture at the total bulk gas phase at 298 K and 1 atm.

Breakthrough simulation properties

It is widely acknowledged that adsorbent performance is determined by metrics of separation ability and adsorption capacity, especially in PSA units. Keeping this in mind, transient breakthrough calculations were conducted. The breakthrough methodologies, with step- or pulse-inputs of gas mixtures, are provided in the ESI.† To demonstrate the fractionation capacity of NACs, we also carried out pulse chromatographic

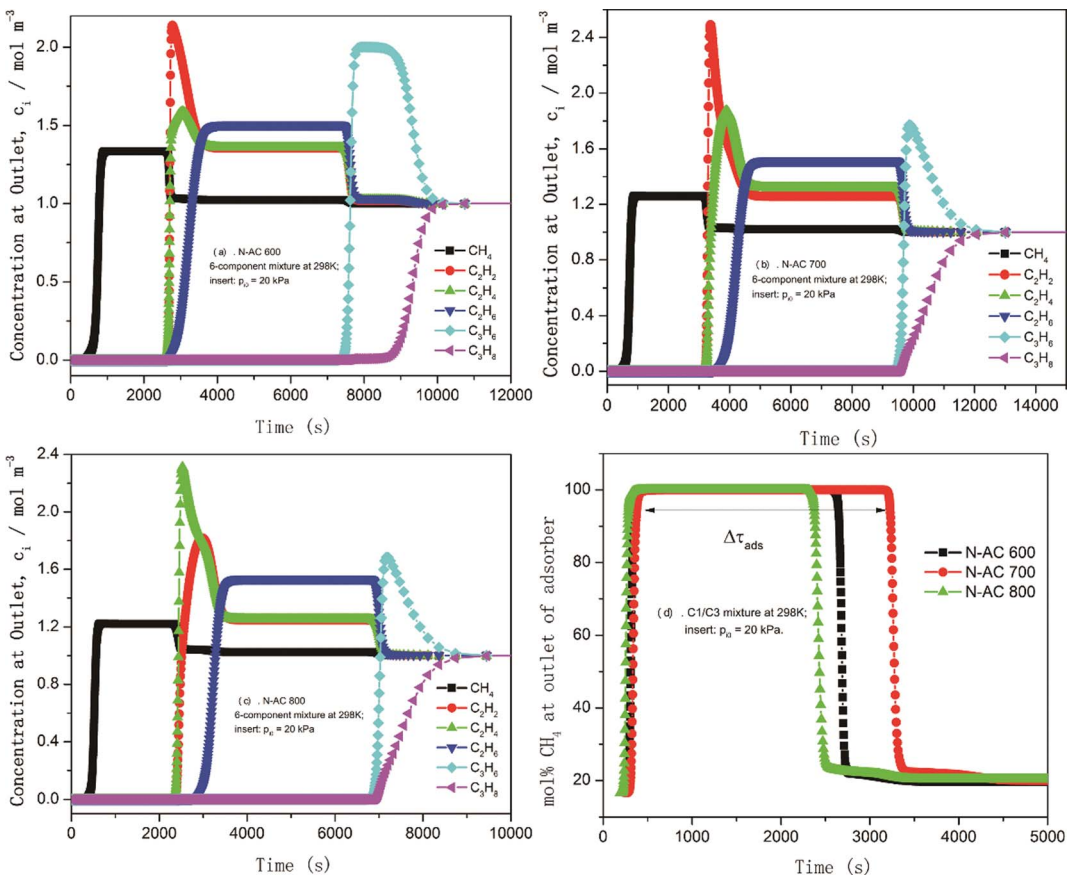

Fig. 10 Breakthrough simulation curves of (a) NAC 600, (b) NAC 700, and (c) NAC 800, for separation of an equimolar 6-component $CH_4/C_2H_2/C_2H_4/C_2H_6/C_3H_6/C_3H_8$ mixture in a fixed adsorber at 298 K and 1 bar, and (d) molar percentage of CH_4 in the exit gas stream as a function of time for NACs.

simulations. The selective adsorption of C2 hydrocarbons from an equimolar 4-component $CH_4/C_2H_2/C_2H_4/C_2H_6$ mixture is first considered. The choice of such a mixture is dictated by the fact that such mixture separation is encountered in the oxidation coupling of the methane process for producing ethylene. The equimolar 4-component $CH_4/C_2H_2/C_2H_4/C_2H_6$ mixture breakthrough curves at 298 K (Fig. 8) clearly showed that the breakthrough time sequence was $C_2H_6 > C_2H_4 \approx C_2H_2 > CH_4$. Three conclusions could be drawn from this observation: (i) NACs could separate CH_4 from quaternary mixtures successfully, the plot of mol% CH_4 in the exit stream as a function of time is presented in Fig. S8;† (ii) except for NAC 600, C_2H_6 could be collected in pure form; (iii) NACs lack the ability to separate C_2H_2–C_2H_4 pairs efficiently. To compare the separation performance of C2/CH_4 on NACs, the C_2H_4/CH_4 mixture pair is chosen due to the fact that C_2H_4 stream took the lead off breaking through the adsorber. The adsorption capacity is dictated by the combined total uptake of C2 light hydrocarbons. Fig. 9 presents C_2H_4/CH_4 IAST selectivity *versus* the total C2 uptake at 298 K and 1 bar. It is worth noting that NAC 700 exhibited the highest selectivity as well as the largest uptake capacity, clearly demonstrating that NAC 700 is the most promising adsorbent in C2/C1 separation. In order to examine the ability to recover each component in nearly pure form, pulse chromatographic simulations for an equimolar 4-component $CH_4/C_2H_2/C_2H_4/C_2H_6$ mixture separation were carried out as well (Fig. S9†). It clearly demonstrated the similar results that it is possible to obtain CH_4 in pure form, but separation of $C_2H_2/C_2H_4/C_2H_6$ is relatively difficult.

To further demonstrate the feasibility of separating 6-component equimolar mixtures, the breakthrough curves are depicted in Fig. 10. In all adsorbers packed with NACs, CH_4 breaks through the earliest due to its poorest adsorption strength, followed by C2 and C3 streams in sequence. Therefore, it is possible to fractionate the bulk mixture stream into three isolated streams according to the carbon atom number. Remarkably, NAC 700 exhibited the best separation performance, no matter whether in the mixture of C1/C2, C1/C3, or C2/C3. Fig. 10d shows that the time interval, $\Delta\tau_{ads}$, of collecting 99%+ CH_4 from the equimolar 6-component mixture, is 2610, 3204, and 2340 seconds for NAC 600, NAC 700, and NAC 800, respectively. This result could be ascribed to the highest C3 adsorption capacity and C3/CH_4 selectivity on NAC 700. Surprisingly, NAC 600 was capable of separating C_3H_6 and C_3H_8, and the breakthrough time interval is 1530 seconds (Fig. S10†). We ascribe this property to the apparent uptake difference (0.72 mmol g^{-1}) between C_3H_6 and C_3H_8 on NAC-600. It is also worth noting that NACs possessed high C_3H_8/C_2H_6 IAST selectivity, shown in Fig. S11,† which is 10.1, 7.6, and 6.3 on NAC-600, NAC 700, and NAC 800, respectively, at 298 K and 1 bar.

4 Conclusion

In summary, we have successfully prepared a series of N-doped (*ca.* 3.6 wt%) porous carbon materials derived from a pre-functionalized polymer precursor for C1/C2/C3 separation. The obtained highly porous materials possessed a hierarchical pore structure with specific surface areas up to 2146.1 m^2 g^{-1} and pore volumes up to 1.96 cm^3 g^{-1}. NACs displayed unprecedented C2 and C3 uptake capacities; particularly, NAC 700 exhibited the highest C_2H_6 and C_3H_8 capacity of 7.59 and 11.77 mmol g^{-1} at 298 K and 1 bar, respectively. Furthermore, excellent IAST selectivity of C2/C1 (*ca.* 65.7) and C3/C1 (*ca.* 501.9) was obtained as well. Meanwhile, NACs possessed high C_3H_8/C_2H_6 IAST selectivity, which is 10.1, 7.6, and 6.3 on NAC-600, NAC 700, and NAC 800, respectively. The *N*-functional groups contribute significantly to enhancement of adsorption capacity and selectivity in two ways: (i) generating a stronger interaction force with polarized hydrocarbon molecules and (ii) adjusting the pore size and architecture. Considering these merits, breakthrough and pulse chromatographic simulations were conducted to further confirm that NACs are potent adsorbents for light hydrocarbon separation.

Acknowledgements

This work is supported by new faculty startup funds from the Fulton Schools of Engineering at ASU. We gratefully acknowledge the use of facilities within the LeRoy Center for Solid State Science and Gold Water Environmental Laboratory and within Prof. Jerry Lin's lab at ASU. We would like to acknowledge the effort made by Han-chun Wu and Joshua James.

References

1 (*a*) Y. He, W. Zhou, G. Qian and B. Chen, *Chem. Soc. Rev.*, 2014, **43**, 5657–5678; (*b*) T. A. Makal, J.-R. Li, W. Lu and H.-C. Zhou, *Chem. Soc. Rev.*, 2012, **41**, 7761–7779.

2 (*a*) A. Miltenburg, J. Gascon, W. Zhu, F. Kapteijn and J. A. Moulijn, *Adsorption*, 2008, **14**, 309–321; (*b*) P. S. Gomes, N. Lamia and A. E. Rodrigues, *Chem. Eng. Sci.*, 2009, **64**, 1336–1357; (*c*) N. A. Al-Baghli and K. F. Loughlin, *J. Chem. Eng. Data*, 2006, **51**, 248–254.

3 M. Shi, A. M. Avila, F. Yang, T. M. Kuznicki and S. M. Kuznicki, *Chem. Eng. Sci.*, 2011, **66**, 2817–2822.

4 (*a*) N. B. K. Magnowski, A. M. Avila, C. C. H. Lin, M. Shi and S. M. Kuznicki, *Chem. Eng. Sci.*, 2011, **66**, 1697–1701; (*b*) R. W. Triebe, F. H. Tezel and K. C. Khulbe, *Gas Sep. Purif.*, 1996, **10**, 81–84.

5 S. Horike, Y. Inubushi, T. Hori, T. Fukushima and S. Kitagawa, *Chem. Sci.*, 2012, **3**, 116–120.

6 (*a*) S. Cavenati, C. A. Grande and A. E. Rodrigues, *Ind. Eng. Chem. Res.*, 2008, **47**, 6333–6335; (*b*) Z.-J. Lin, T.-F. Liu, Y.-B. Huang, J. Lü and R. Cao, *Chem.–Eur. J.*, 2012, **18**, 7896–7902; (*c*) J. R. Li, R. J. Kuppler and H. C. Zhou, *Chem. Soc. Rev.*, 2009, **38**, 1477–1504.

7 (*a*) Y. B. He, R. Krishna and B. L. Chen, *Energy Environ. Sci.*, 2012, **5**, 9107–9120; (*b*) H. Xu, J. Cai, S. Xiang, Z. Zhang, C. Wu, X. Rao, Y. Cui, Y. Yang, R. Krishna, B. Chen and G. Qian, *J. Mater. Chem. A*, 2013, **1**, 9916–9921; (*c*) L. Li, X. Wang, J. Liang, Y. Huang, H. Li, Z. Lin and R. Cao, *ACS Appl. Mater. Interfaces*, 2016, **8**, 9777–9781; (*d*) L. Li,

R. Krishna, Y. Wang, J. Yang, X. Wang and J. Li, *J. Mater. Chem. A*, 2016, **4**, 751–755.

8 (*a*) E. D. Bloch, W. L. Queen, R. Krishna, J. M. Zadrozny, C. M. Brown and J. R. Long, *Science*, 2012, **335**, 1606–1610; (*b*) T.-L. Hu, H. Wang, B. Li, R. Krishna, H. Wu, W. Zhou, Y. Zhao, Y. Han, X. Wang, W. Zhu, Z. Yao, S. Xiang and B. Chen, *Nat. Commun.*, 2015, **6**, 7328.

9 (*a*) B. Li, Y. Zhang, R. Krishna, K. Yao, Y. Han, Z. Wu, D. Ma, Z. Shi, T. Pham, B. Space, J. Liu, P. K. Thallapally, J. Liu, M. Chrzanowski and S. Ma, *J. Am. Chem. Soc.*, 2014, **136**, 8654–8660; (*b*) S. Yang, A. J. Ramirez-Cuesta, R. Newby, V. Garcia-Sakai, P. Manuel, S. K. Callear, S. I. Campbell, C. C. Tang and M. Schröder, *Nat. Chem.*, 2015, **7**, 121–129.

10 J. Duan, W. Jin and R. Krishna, *Inorg. Chem.*, 2015, **54**, 4279–4284.

11 J. Jia, L. Wang, F. Sun, X. Jing, Z. Bian, L. Gao, R. Krishna and G. Zhu, *Chem.–Eur. J.*, 2014, **20**, 9073–9080.

12 (*a*) B. Yuan, X. F. Wu, Y. X. Chen, J. H. Huang, H. M. Luo and S. G. Deng, *Environ. Sci. Technol.*, 2013, **47**, 5474–5480; (*b*) J. Wang, R. Krishna, X. Wu, Y. Sun and S. Deng, *Langmuir*, 2015, **31**, 9845–9852; (*c*) J. Wang, R. Krishna, J. Yang, K. P. R. Dandamudi and S. Deng, *Materials Today Communications*, 2015, **4**, 156–165.

13 (*a*) S. M. Mahurin, J. Górka, K. M. Nelson, R. T. Mayes, S. Dai, J. Gorka, K. M. Nelson, R. T. Mayes, S. Dai, J. Górka, K. M. Nelson, R. T. Mayes and S. Dai, *Carbon*, 2014, **67**, 457–464; (*b*) J. Wang, R. Krishna, J. Yang and S. Deng, *Environ. Sci. Technol.*, 2015, **49**, 9364–9373.

14 W. Xia, B. Qiu, D. G. Xia and R. Q. Zou, *Sci. Rep.*, 2013, **3**, 1935.

15 H. Bux, C. Chmelik, R. Krishna and J. Caro, *J. Membr. Sci.*, 2011, **369**, 284–289.

16 B. Yuan, J. Wang, Y. Chen, X. Wu, H. Luo and S. Deng, *J. Mater. Chem. A*, 2016, **4**, 2263–2276.

17 Y. B. He, W. Zhou, R. Krishna and B. L. Chen, *Chem. Commun.*, 2012, **48**, 11813–11831.

18 W. Chaikittisilp, A. Sugawara, A. Shimojima and T. Okubo, *Chem. Mater.*, 2010, **22**, 4841–4843.

19 C. Wang, Y. Wang, J. Graser, R. Zhao, F. Gao and M. J. O'Connell, *ACS Nano*, 2013, **7**, 11156–11165.

20 K. P. Gierszal, M. Jaroniec, T.-W. Kim, J. Kim and R. Ryoo, *New J. Chem.*, 2008, **32**, 981–993.

21 M. Saleh, J. N. Tiwari, K. C. Kemp, M. Yousuf and K. S. Kim, *Environ. Sci. Technol.*, 2013, **47**, 5467–5473.

22 L. G. Cançado, K. Takai, T. Enoki, M. Endo, Y. A. Kim, H. Mizusaki, A. Jorio, L. N. Coelho, R. Magalhães-Paniago and M. A. Pimenta, *Appl. Phys. Lett.*, 2006, **88**, 163106.

23 T. Lin, I.-W. Chen, F. Liu, C. Yang, H. Bi, F. Xu and F. Huang, *Science*, 2015, **350**, 1508–1513.

24 L. Hao, X. Li and L. Zhi, *Adv. Mater.*, 2013, **25**, 3899–3904.

25 K. S. W. Sing, D. H. Everett, R. a. W. Haul, L. Moscou, R. a. Pierotti, J. Rouquérol and T. Siemieniewska, *Pure Appl. Chem.*, 1985, **57**, 603–619.

26 R. Krishna and J. R. Long, *J. Phys. Chem. C*, 2011, **115**, 12941–12950.

27 (*a*) Y. He, Z. Zhang, S. Xiang, F. R. Fronczek, R. Krishna and B. Chen, *Chem.–Eur. J.*, 2012, **18**, 613–619; (*b*) D. Wang, B. Liu, S. Yao, T. Wang, G. Li, Q. Huo and Y. Liu, *Chem. Commun.*, 2015, **51**, 15287–15289; (*c*) D. Wang, T. Zhao, Y. Cao, S. Yao, G. Li, Q. Huo and Y. Liu, *Chem. Commun.*, 2014, **50**, 8648–8650.

28 Y. Huang, Z. Lin, H. Fu, F. Wang, M. Shen, X. Wang and R. Cao, *ChemSusChem*, 2014, **7**, 2647–2653.

Electronic Supplementary Material (ESI) for Journal of Materials Chemistry A.

Supporting Material

A Novel Class of Nitrogen-rich Microporous Carbons for Highly Selective Separation of Light Hydrocarbons

Jun Wang [ab], Rajamani Krishna [c], Ting Yang [b], Shuguang Deng [ab] *

[a.] School of Environmental and Chemical Engineering,
Nanchang University,
Nanchang 330031, Jiangxi, PR China

[b.] School for Engineering of Matter, Transport and Energy
Arizona State University
531 E. Tyler Mall, Tempe, AZ, 85287, USA

[c.] van't Hoff Institute for Molecular Sciences
University of Amsterdam
Science Park 904, 1098 XH Amsterdam, The Netherlands

*Corresponding author: Tel: +1-575-646-4346.

E-mail address: shuguang.deng@asu.edu

Contents

Figure S1. Schematic illustration of synthesis process.

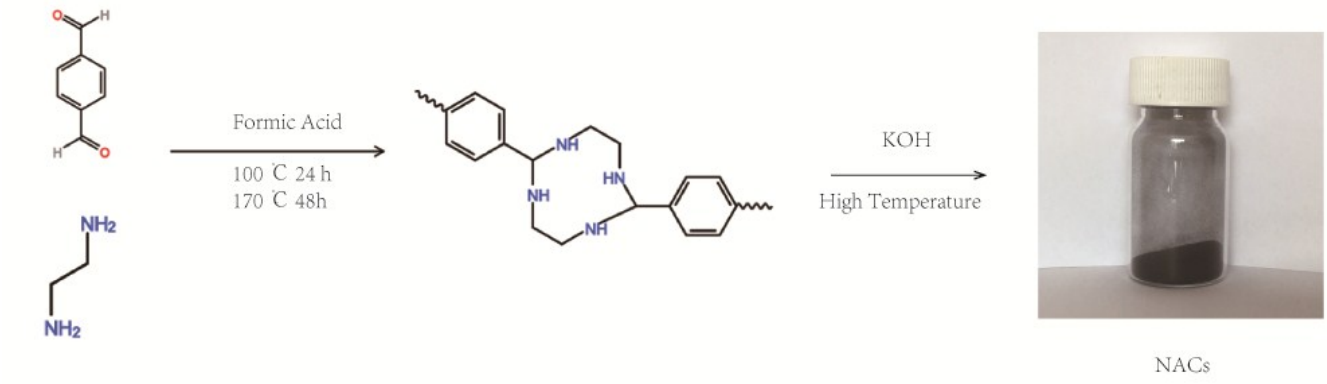

{Figure S1}

Figure S2. Wide XRD spectra of NACs.

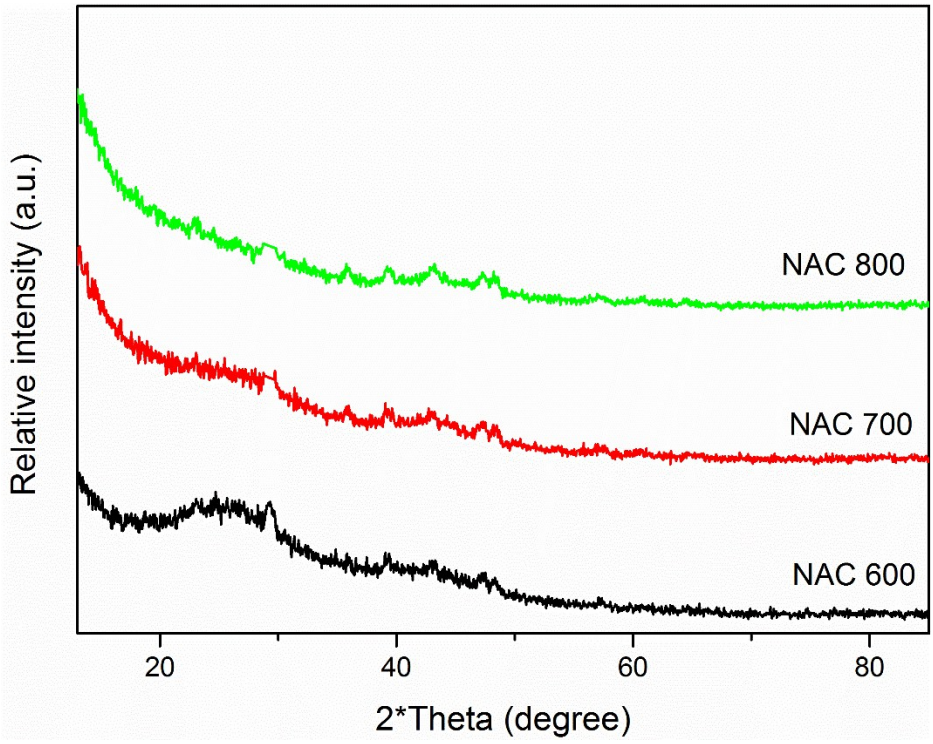

{Figure S2}

Figure S3. TGA and DTG curves of (a). NAC 600, (b). NAC 700, and (c). NAC 800.

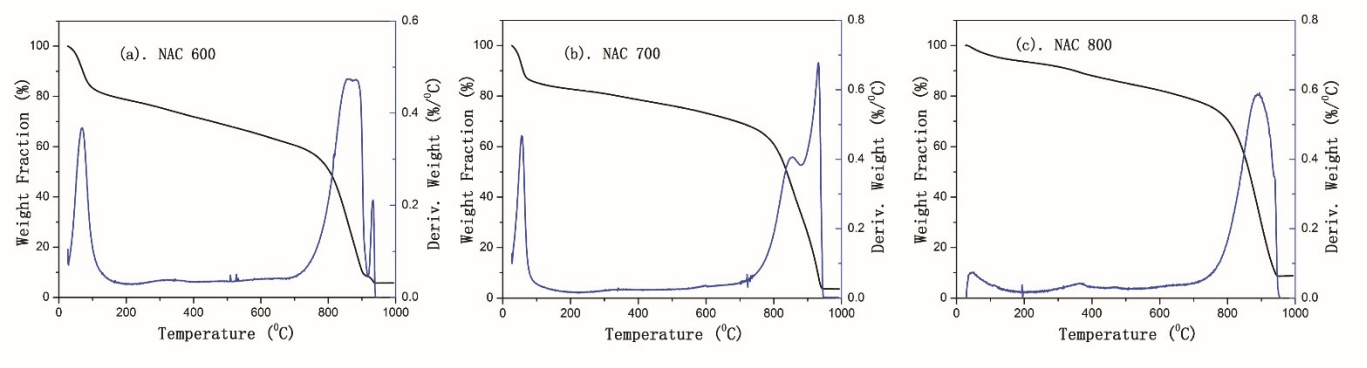

{Figure S3}

Figure S4. C 1s spectra for (a) NAC 600, (b) NAC 700, and (c) NAC 800.

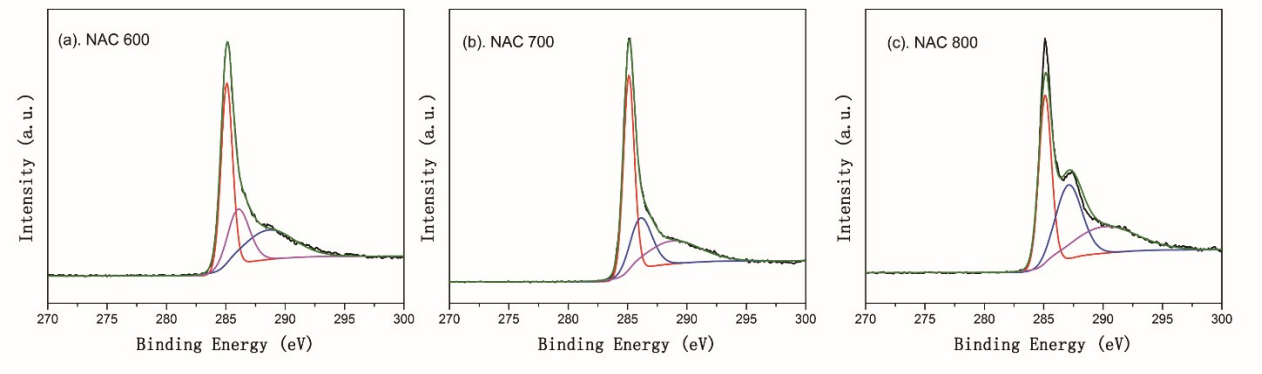

{Figure S4}

Figure S5. Light hydrocarbons adsorption isotherms on (a) NAC 600, (b) NAC 700, (c) NAC 800 at 323 K and 1 bar.

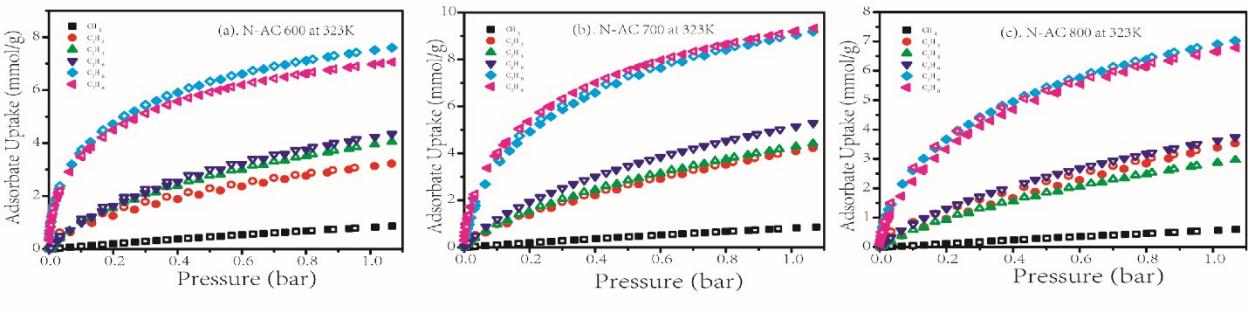

{Figure S5}

Fitting of pure component isotherms

The experimentally measured loadings for CH_4, C_2H_2, C_2H_4, C_2H_6, C_3H_6, and C_3H_8 were measured as a function of the absolute pressure at three different temperatures 273 K, 298 K, and 323 K.

The unary isotherm data for each guest molecule were fitted with the Langmuir-Freundlich model

$$q = q_{sat} \frac{bp^{\nu}}{1 + bp^{\nu}} \tag{1}$$

with T-dependent parameter b

$$b = b_0 \exp\left(\frac{E}{RT}\right) \tag{2}$$

The Langmuir-Freundlich parameters for adsorption of CH_4, C_2H_2, C_2H_4, C_2H_6, C_3H_6, and C_3H_8 are provided in Tables S1, S2, and S3 for NAC 600, NAC 700, and NAC 800, respectively. For all guest/host combinations the isotherm fits are excellent.

Table S1. Langmuir-Freundlich parameters for adsorption of CH_4, C_2H_2, C_2H_4, C_2H_6, C_3H_6, and C_3H_8 in NAC 600.

	q_{sat} mol kg^{-1}	b_0 Pa$^{-\nu}$	E kJ mol^{-1}	ν dimensionless
CH_4	4.9	2.28×10^{-9}	18.2	1
C_2H_2	12	4.38×10^{-7}	17	0.63
C_2H_4	9.2	1.8×10^{-9}	23.7	0.96
C_2H_6	9.9	7.04×10^{-9}	22	0.9
C_3H_6	12.7	3.12×10^{-6}	14.3	0.69
C_3H_8	12	4.77×10^{-6}	17.4	0.53

{Table S1}

Table S2. Langmuir-Freundlich parameters for adsorption of CH_4, C_2H_2, C_2H_4, C_2H_6, C_3H_6, and C_3H_8 in NAC 700.

	q_{sat} mol kg^{-1}	b_0 Pa$^{-\nu}$	E kJ mol^{-1}	ν dimensionless
CH_4	5.4	2.73×10^{-9}	17.4	1
C_2H_2	33.7	1.56×10^{-7}	15.7	0.68
C_2H_4	15.6	7.81×10^{-8}	18.1	0.75

C_2H_6	16.5	5.79×10^{-9}	18.8	0.77
C_3H_6	17.6	5.23×10^{-7}	19.8	0.62
C_3H_8	17	1.62×10^{-6}	18	0.59

{Table S2}

Table S3. Langmuir-Freundlich parameters for adsorption of CH_4, C_2H_2, C_2H_4, C_2H_6, C_3H_6, and C_3H_8 in NAC 800.

	q_{sat} mol kg^{-1}	b_0 $Pa^{-\nu}$	E kJ mol^{-1}	ν dimensionless
CH_4	4.9	1.84×10^{-9}	17.7	1
C_2H_2	17	1.28×10^{-8}	17.6	0.89
C_2H_4	10.5	1.62×10^{-8}	19	0.86
C_2H_6	13.7	5.33×10^{-8}	18.4	0.77
C_3H_6	16	2.95×10^{-6}	14.4	0.62
C_3H_8	13.3	1.23×10^{-7}	22.3	0.66

{Table S3}

Figure S6. Regeneration ability on N-AC 700 at 298 K and 1 bar.

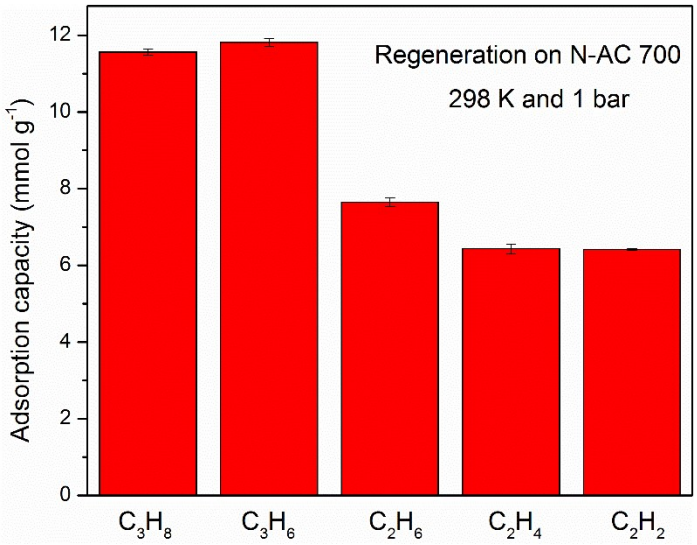

{Figure S6}

Figure S7. Adsorption heat of light hydrocarbons on (a) NAC 600, (b) NAC 700, (c) NAC 800.

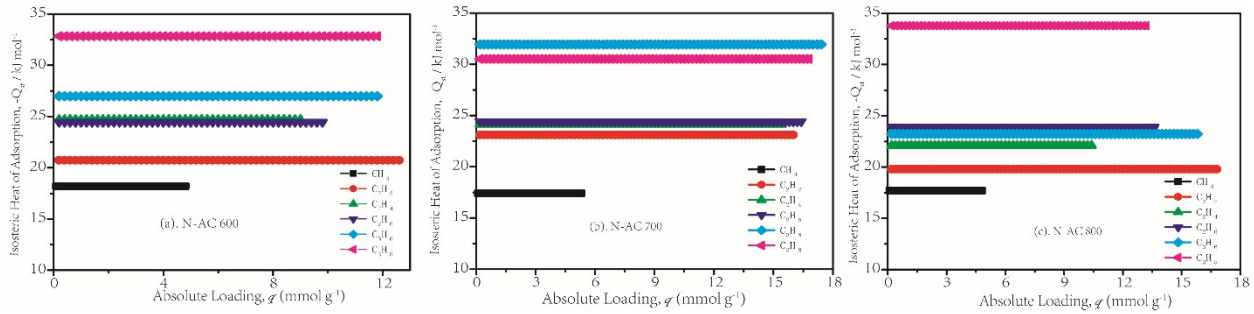

{Figure S7}

Table S4. Comparison of C_3H_8/CH_4, C_3H_6/CH_4, C_2H_6/CH_4, C_2H_4/CH_4, and C_2H_2/CH_4 selectivities of NAC 700 with other benchmark adsorbents.

Samples	C_3H_8/CH_4	C_3H_6/CH_4	C_2H_6/CH_4	C_2H_4/CH_4	C_2H_2/CH_4	References
NAC 700	501.9	419.8	65.7	45.1	47.1	This work
FJI-C4	293.4	-	39.7	22.1	51.0	1

UTSA-35a	80	-	13.5	8	19	2
UTSA-33a	-	-	16	12	18	3
JLU-Liu22	271.5	-	14.4	-	-	4
JLU-Liu5	107.8	-	17.6	-	-	5
JLU-Liu6	274.6	-	20.4	-	-	6
JLU-Liu18	108.2	-	13.1	-	-	7

{Table S4}

Figure S8. Mole percentage of CH_4 in the exit gas stream as a function of time for NACs.

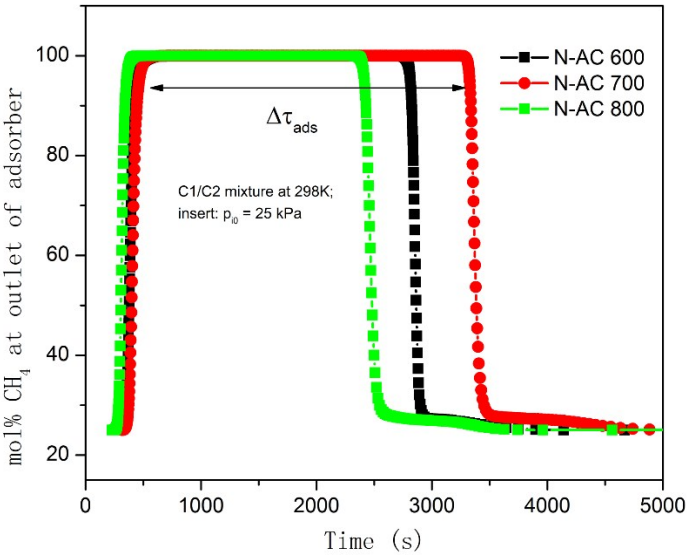

{Figure S8}

Figure S9. Pulse chromatographic simulations for separation of an equimolar 4-component $CH_4/C_2H_2/C_2H_4/C_2H_6$ mixture on (a) NAC 600, (b) NAC 700, and (c) NAC 800 at 298 K and 1 bar.

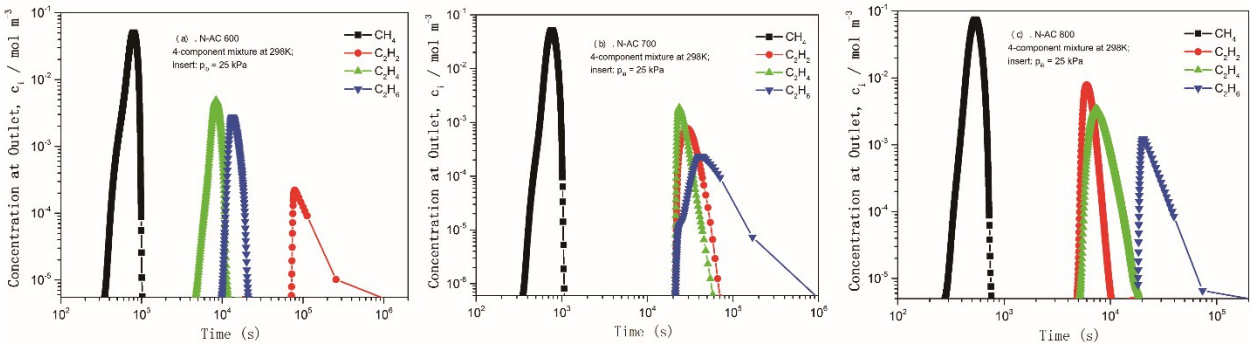

{Figure S9}

Figure S10. IAST calculations of C3/C1 and C2/C1 in an equimolar 6-component $CH_4/C_2H_2/C_2H_4/C_2H_6/C_3H_6/C_3H_8$ mixture on (a) NAC 600, (a) NAC 700, and (a) NAC 800 at 298 K and 1 bar.

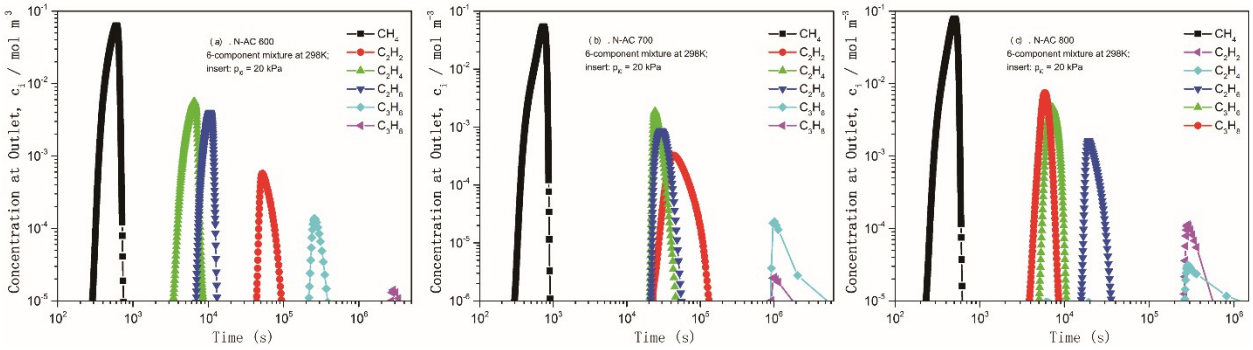

{Figure S10}

Figure S11. C_3H_6/C_2H_6 IAST calculations on NACs.

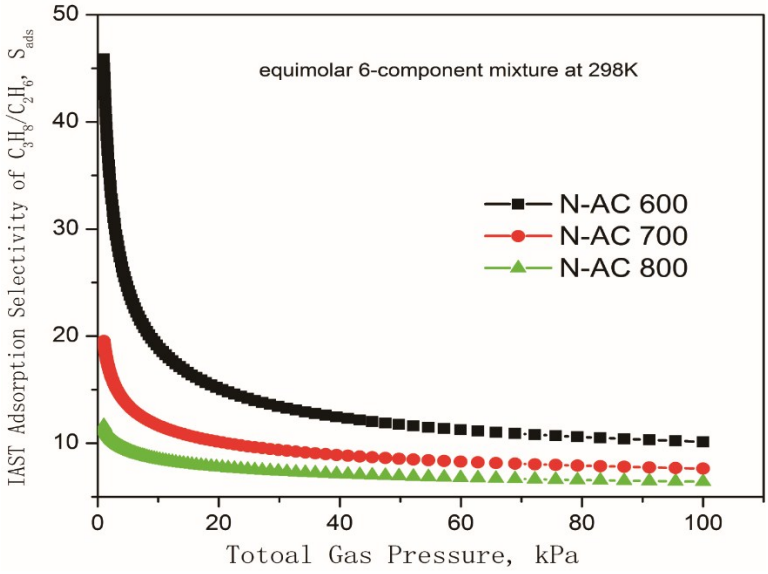

{Figure S11}

Transient breakthroughs in fixed bed adsorber

A brief summary of the breakthrough simulation methodology, essentially the same as that presented by Krishna [8,9], is provided below.

Assuming plug flow of an *n*-component gas mixture through a fixed bed maintained under isothermal conditions, the partial pressures in the gas phase at any position and instant of time are obtained by solving the following set of partial differential equations for each of the species *i* in the gas mixture.

$$\frac{1}{RT}\frac{\partial p_i(t,z)}{\partial t} = -\frac{1}{RT}\frac{\partial\left(v(t,z)p_i(t,z)\right)}{\partial z} - \frac{(1-\varepsilon)}{\varepsilon}\rho\frac{\partial \bar{q}_i(t,z)}{\partial t}; \quad i = 1,2,...n \tag{3}$$

In equation (3), t is the time, z is the distance along the adsorber, ρ is the framework density, ε is the bed voidage, v is the interstitial gas velocity, and $\bar{q}_i(t,z)$ is the *spatially averaged* molar loading within the crystallites of radius r_c, monitored at position z, and at time t.

At any time t, during the transient approach to thermodynamic equilibrium, the spatially averaged molar loading within the crystallite r_c is obtained by integration of the radial loading profile

$$\bar{q}_i(t) = \frac{3}{r_c^3}\int_0^{r_c} q_i(r,t) r^2 dr \tag{4}$$

For the breakthrough simulations presented in this article, we assume that intra-crystalline diffusion is of negligible importance. With this assumption the entire crystallite particle can be considered to be in thermodynamic equilibrium with the surrounding bulk gas phase at that time t, and position z of the adsorber

$$\bar{q}_i(t,z) = q_i(t,z) \tag{5}$$

The molar loadings at any position z, at time t in Equation (5) are calculated on the basis of adsorption equilibrium with the bulk gas phase partial pressures p_i at that position z and time t. The adsorption equilibrium can be calculated on the basis of the Ideal Adsorbed Solution Theory (IAST) of Myers and Prausnitz [10]. In all the simulation results we present in this article, the IAST calculations use Langmuir-Freundlich isotherm fits.

The *interstitial* gas velocity is related to the *superficial* gas velocity by

$$v = \frac{u}{\varepsilon} \tag{6}$$

In industrial practice, the most common operation is with to use a step-wise input of mixtures to be separation into an adsorber bed that is initially free of adsorbates, i.e. we have the initial condition

$$t = 0; \quad q_i(0,z) = 0 \tag{7}$$

At time, $t = 0$, the inlet to the adsorber, $z = 0$, is subjected to a step input of the n-component gas mixture and this step input is maintained till the end of the adsorption cycle when steady-state conditions are reached.

$$t \geq 0; \quad p_i(0,t) = p_{i0}; \quad u(0,t) = u \tag{8}$$

where u is the superficial gas velocity at the inlet to the adsorber.

Besides, the breakthrough simulations with a step-input (8), we also carried out simulations for a packed bed adsorber with injection of a short duration pulse of the mixture to be separated. This type of simulation is particularly useful to demonstrate the fractionating capability of adsorbents. For simulation of pulse chromatographic separations, we use the corresponding set of inlet conditions

$$0 \leq t \leq t_0; \quad p_i(0,t) = p_{i0}; \quad u(0,t) = u \tag{9}$$

where the time for duration of the pulse is t_0.

In order to evaluate the different N-ACs, breakthrough calculations were performed taking the following parameter values: inside diameter of tube = 50 mm; bed length, L = 1.8 m; voidage of bed, ε = 0.5; superficial gas velocity, u = 0.05 m/s (at inlet), interstitial velocity, v = 0.1 m/s. The mass of adsorbent packed in the tube is 2 kg. For the pulse chromatographic simulations, a pulse injection time t_0 = 10 s was used. We use the dimensionless time, $\tau = \frac{tu}{L\varepsilon}$, obtained by dividing the actual time, t, by the characteristic time, $\frac{L\varepsilon}{u}$, when plotting simulated breakthrough curves [8].

Notation

b	Langmuir-Freundlich constant for species *i* at adsorption site A, $\mathrm{Pa}^{-\nu}$
c_i	molar concentration of species *i* in gas mixture, mol m^{-3}
c_{i0}	molar concentration of species *i* in gas mixture at inlet to adsorber, mol m^{-3}
E	energy parameter, J mol^{-1}
L	length of packed bed adsorber, m
p_i	partial pressure of species *i* in mixture, Pa
p_t	total system pressure, Pa
q_i	component molar loading of species *i*, mol kg^{-1}
Q_{st}	isosteric heat of adsorption, J mol^{-1}
R	gas constant, 8.314 J mol^{-1} K^{-1}
t	time, s
T	absolute temperature, K
u	superficial gas velocity in packed bed, m s^{-1}

Greek letters

ε	voidage of packed bed, dimensionless
ρ	framework density, kg m^{-3}
ν	Freundlich exponent, dimensionless
τ	time, dimensionless

References

[1] Li L, Wang X, Liang J, Huang Y, Li H, Lin Z, et al. Water-Stable Anionic Metal–Organic Framework for Highly Selective Separation of Methane from Natural Gas and Pyrolysis Gas. ACS Appl Mater Interfaces 2016.

[2] Krishna R, Long JR. Screening Metal-Organic Frameworks by Analysis of Transient Breakthrough of Gas Mixtures in a Fixed Bed Adsorber. J Phys Chem C 2011;115:12941–50.

[3] He Y, Zhang Z, Xiang S, Fronczek FR, Krishna R, Chen B. A Microporous Metal–Organic Framework for Highly Selective Separation of Acetylene, Ethylene, and Ethane from Methane at Room Temperature. Chem – A Eur J 2012;18:613–9.

[4] Wang D, Liu B, Yao S, Wang T, Li G, Huo Q, et al. A polyhedral metal-organic framework based on the supermolecular building block strategy exhibiting high performance for carbon dioxide capture and separation of light hydrocarbons. Chem Commun 2015;51:15287–9.

[5] Wang D, Zhao T, Cao Y, Yao S, Li G, Huo Q, et al. High performance gas adsorption and separation of natural gas in two microporous metal-organic frameworks with ternary building units. Chem Commun 2014;50:8648–50.

[6] Yao S, Wang D, Cao Y, Li G, Huo Q, Liu Y. Two stable 3D porous metal–organic frameworks with high performance for gas adsorption and separation. J Mater Chem A 2015;3:16627–32.

[7] Myers, A. L.; Prausnitz, J. M. Thermodynamics of Mixed Gas Adsorption, *A.I.Ch.E.J.* **1965**, *11*, 121-130.

[8] Krishna, R. Methodologies for Evaluation of Metal-Organic Frameworks in Separation Applications, *RSC Adv.* **2015**, *5*, 52269-52295.

[9] Krishna, R. The Maxwell-Stefan Description of Mixture Diffusion in Nanoporous Crystalline Materials, *Microporous Mesoporous Mater.* **2014**, *185*, 30-50.